Research Square

Preprints are preliminary reports that have not undergone peer review.
They should not be considered conclusive, used to inform clinical practice,
or referenced by the media as validated information.

Stability window and band-gap tuning in trigonal Cu2SrGeS4−xSex (x = 0–4): a first-principles GGA+U study

Slamnia Djamel
Laboratory for the Development and Physicomechanical and Metallurgical Characterization of Materials (ECP3M),
Boukortt Abdelkader
Laboratory for the Development and Physicomechanical and Metallurgical Characterization of Materials (ECP3M),
Beloufa Nabil
beloufa.nabil@gmail.com

Hydrometeorological Institute for Training and Research IHFR
Hadjar Hakima
Laboratory for the Development and Physicomechanical and Metallurgical Characterization of Materials (ECP3M),
Meskine Said
Laboratory for the Development and Physicomechanical and Metallurgical Characterization of Materials (ECP3M),

Research Article

Keywords: Cu2SrGeS4, chalcogenide alloys, thermodynamic stability, GGA + U, FP-LAPW + lo, photovoltaic absorber

Posted Date: November 20th, 2026

DOI: https://doi.org/10.21203/rs.3.rs-11609967/v1

License: This work is licensed under a Creative Commons Attribution 4.0 International License.
Read Full License

Additional Declarations: No competing interests reported.

Stability window and band-gap tuning in trigonal $Cu_2SrGeS_{4-x}Se_x$ (x = 0–4): a first-principles GGA+*U* study

Slamnia Djamel[1] , Boukortt Abdelkader[1] , Beloufa Nabil[2,3], Hadjar Hakima[1], Meskine Said[1]

[1] *Laboratory for the Development and Physicomechanical and Metallurgical Characterization of Materials (ECP3M), Abdelhamid Ibn Badis University, National Highway No. 11, Kharouba, 27000 Mostaganem, Algeria.*

[2] *Hydrometeorological Institute for Training and Research IHFR, Ibnou Rochd.Bp 7019,Oran Algeria*

[3] *Laboratory o f Micro and Nanophysics (LaMiN), National Polytechnic School Oran, ENPO-MA,BP1523, El M'Naouer , 31000, Oran, Algeria*

Abstract

Cu_2SrGeS_4 is a member of the trigonal I_2–II–IV–VI_4 chalcogenide family, which has been proposed as a readily available absorber on Earth that avoids the cationic disorder found in kestrites. In this study, we investigated how the complete S→Se substitution alters its thermodynamic stability, electronic structure, and optical response. We used full-electron FP-LAPW+lo calculations, applying the GGA-PBE method for structural properties, and the GGA+U method (U = 3.95 eV on Cu 3d) for electronic and optical properties. The PBE lattice parameters of the Cu_2SrGeS_4 compound agree with experimental results to within 1.1%. The substitution results in an anisotropic expansion of the lattice, by 4.0% along the a-axis and 8.8% along the c-axis for x = 4. All compounds exhibit a negative enthalpy of formation, ranging from −0.82 to −0.70 eV/atom. Compared to the competing phases Cu_2GeS_3, Cu_2GeSe_3, SrS, and SrSe, however, the trigonal structure is favored only on the S-rich side.

The reaction energy increases from −14.5 meV/atom at x = 0 to +16.3 meV/atom at x = 4 and changes sign around x ≈ 1.6, while the mixing enthalpy of the ordered alloys remains below 1.2 meV/atom. At x = 4, the orthorhombic Ama2 structure exhibits an energy that is at least 11.8 meV/atom lower, which is consistent with experimental results. The GGA+U bandgap is nearly direct for all compositions and narrows from 1.36 to 0.58 eV, with a curvature parameter of 0.12 eV. The conduction electrons are light (0.08–0.21 m_0), and the zz absorption threshold lies between 0.12 and 0.22 eV above the xx threshold. For x ≤ 2, the calculated band gaps yield detailed-equilibrium efficiency limits ranging from 31 to 34%, and the trigonal phase remains thermodynamically favored up to x ≈ 1.6.

Keywords: Cu_2SrGeS_4 ; chalcogenide alloys; thermodynamic stability; GGA+U; FP-LAPW+lo; photovoltaic absorber.

1. Introduction

The chalcogenide compounds are among of materials witch proposed for the development of new solar cells. Their high optical absorption coefficient makes them candidate replacements for absorbers that raise toxicity concerns, such as lead in perovskite cells [1], or that rely on scarce and costly elements, such as indium and gallium in Cu(In,Ga)Se_2 (CIGS) cells [2,3].Whether a new material can serve as an absorber layer depends first on its band structure. Its band gap must lie in the optimal range for absorbing the solar spectrum, between 1.1 and 1.5 eV [4], so that charge carriers are generated and transported efficiently.

Theoretical calculations on these compounds become difficult when they contain transition-metal elements with localized d orbitals. Standard approximations of density functional theory, such as the generalized gradient approximation (GGA), fail to treat the strong electron correlations within these orbitals. This methodological shortcoming yields band gaps smaller than the experimental values and degrades the accuracy of the derived optical properties [5,6]. It therefore limits the reliability of the predicted material properties.

Among chalcogenide absorbers, kesterite $Cu_2ZnSn(S,Se)_4$ contains only abundant and non-toxic elements. Its efficiency, however, is limited by a large open-circuit voltage deficit. This deficit has been linked to the low formation energy of Cu–Zn antisites and their defect complexes, which arises from the similar size and tetrahedral coordination of Cu^+ and Zn^{2+} [7,8].One way to suppress this disorder is to replace Zn^{2+} by a much larger alkaline-earth cation. Ba^{2+} and Sr^{2+} do not fit the tetrahedral sites of the kesterite lattice. The resulting I_2–II–IV–VI_4 compounds therefore crystallize in other structures, most often trigonal ($P3_1$ or $P3_2$), in which the alkaline-earth ion is eightfold coordinated and Cu–II antisites are energetically costly [9,10]. Hybrid-functional calculations predicted direct or nearly direct gaps for most Cu-based members of this family [10]. $Cu_2BaSn(S,Se)_4$ absorbers have since reached device efficiencies above 5% [11]. The spectroscopy of Cu_2SrSnS_4 and Cu_2BaSnS_4 [12] and the band alignment of Cu_2SrSnS_4 [13] have also been studied. The group-IV cation offers a second handle: replacing Sn by Ge raises the conduction-band minimum and widens the gap, and Ge/Sn alloying tunes the gap continuously [14].

Cu_2SrGeS_4 was first synthesized by Teske, who solved its structure in the trigonal space group $P3_2$ with three formula units per cell [15]. Its optical gap was later estimated at 2.8 eV from diffuse reflectance (the compound is written $SrCu_2GeS_4$ in that work) [16]. The end members Cu_2SrGeS_4 and $Cu_2SrGeSe_4$ have been treated in a first-principles survey of XCu_2GeQ_4 compounds [17]. The Se end member, however, is reported in the orthorhombic space group Ama2 rather than in $P3_2$ [18,19]. A comparable change from trigonal to orthorhombic symmetry has been observed at high Se content in $BaCu_2Sn(S,Se)_4$ [20]. S→Se substitution in Cu_2SrGeS_4 therefore raises two questions: how far the gap can be tuned, and up to which composition the trigonal structure survives.

The gap of the sulfide is too wide for a single-junction absorber. In kesterites and in $BaCu_2Sn(S,Se)_4$, partial replacement of S by Se lowers the gap, because the Se 4p states lie higher than the S 3p states and raise the valence-band maximum [21,22]. A similar narrowing is expected for $Cu_2SrGeS_{4-x}Se_x$. To our knowledge, however, the intermediate compositions have not been studied, and their stability against decomposition into binary and ternary chalcogenides is not known. Both points must be settled before the series can be assessed as an absorber family.

In this work, we studied the full series $Cu_2SrGeS_{4-x}Se_x$ ($x = 0–4$) in the trigonal $P3_2$ structure with the all-electron FP-LAPW+lo method. We first optimized the structures with GGA-PBE and computed three energies that probe stability at different levels: the formation enthalpy from the elements, the reaction energy against the competing phases Cu_2GeS_3, Cu_2GeSe_3, SrS and SrSe, and the mixing enthalpy of the alloys. We also compared the trigonal and orthorhombic polymorphs at both ends of the series. We then computed the band structures, densities of states, effective masses and linear optical spectra within GGA+U. Finally, we used the computed gaps to evaluate the detailed-balance efficiency limit across the series. These results define a composition window in which the trigonal phase is thermodynamically favoured and its gap stays close to the optimum.

2. Computational methods

2.1. Electronic-structure method

We performed all calculations with the full-potential linearized augmented plane wave plus local orbitals (FP-LAPW+lo) method implemented in WIEN2k [23], using the PBE generalized gradient approximation [24] for exchange and correlation. The muffin-tin radii were 2.50, 2.12, 2.05 and 1.74 bohr for Sr, Cu, Ge and S/Se, respectively. The plane-wave cutoff was $R_{MT}\cdot K_{max} = 7.0$ for

the smallest sphere, i.e. K_{max} = 4.02 bohr^{-1}. We kept the same K_{max}, the same sphere radius for each element and the same radial mesh (781 points) in every compound and reference phase, so that basis-set errors cancel in the energy differences of Section 3. The charge density was expanded up to G_{max} = 12 bohr^{-1}, and the non-spherical components inside the spheres up to l_{max} = 10. Brillouin-zone integrations for the 24-atom cells used a 12 × 12 × 4 k-mesh in the full zone. For the reference phases, we increased the k-mesh until the total energy changed by less than 0.05 mRy per cell. Self-consistency was reached when the total energy and the charge changed by less than 10^{-4} Ry and 10^{-3} e between iterations. All compounds are closed-shell (Cu^{+} $3d^{10}$, Ge^{4+}), and the calculations were non-magnetic. Spin–orbit coupling was not included.

2.2. Structures and Se ordering

We modelled the parent compound in its experimental $P3_2$ cell (No. 145) with Z = 3, i.e. 24 atoms [15]. This cell contains four symmetry-inequivalent anion sites, each of multiplicity three. We generated the intermediate compositions x = 1, 2 and 3 by placing Se on one, two and three of these sites, i.e. on 3, 6 and 9 of the 12 anion positions . This choice keeps the $P3_2$ symmetry and gives one ordered configuration per composition. For each composition, we optimized the volume and the c/a ratio by fitting the total energy to the Murnaghan equation of state [25]. We then relaxed the internal coordinates with the MSR1a algorithm [26] until the residual forces fell below 1 mRy/bohr. All structures and total energies were obtained with PBE alone, without a Hubbard term.

2.3. GGA+U and band-gap analysis

Semilocal functionals place the occupied Cu 3d states too high and overestimate their repulsion with the anion p states, which pushes the valence-band maximum up and narrows the gap [5,27]. We therefore computed the electronic and optical properties within GGA+U [28,29], at the PBE geometries. We applied an on-site term U = 0.29 Ry (3.95 eV) to the Cu 3d states, with J = 0 and the fully localized-limit double counting; with J = 0 this is equivalent to the effective-U scheme of Dudarev et al. [30]. This value is close to the effective U ≈ 4 eV derived for the Cu 3d states of Cu-based multinary chalcogenides [6]. We did not fit it to the measured optical gap, and we used the same U for all compositions. Band structures were computed along Γ–M–K–Γ–A–L–H–A.

We obtained the effective masses from parabolic fits to the band extrema, in the basal plane ($m_{\perp}$) and along the c axis ($m_{\parallel}$). The effective densities of states of the conduction and valence bands follow as:

$$N_{c,v} = 2\left(\frac{2\pi m^{*}_{\mathrm{dos}} k_B T}{h^2}\right)^{3/2}, \qquad m^{*}_{\mathrm{dos}} = \left(m_{\perp}^2\, m_{\parallel}\right)^{1/3}, \qquad (1)$$

at T = 300 K. N_v includes the two highest valence bands.

2.4. Thermodynamic quantities

We computed the formation enthalpy per atom from the total energy E(x) of one formula unit (eight atoms) and the chemical potentials μ_i of the elements in their standard phases:

$$\Delta H_f(x) = \frac{1}{8}\left[E(x) - 2\mu_{\mathrm{Cu}} - \mu_{\mathrm{Sr}} - \mu_{\mathrm{Ge}} - (4-x)\,\mu_{\mathrm{S}} - x\,\mu_{\mathrm{Se}}\right]. \qquad (2)$$

The references were fcc Cu, fcc Sr, diamond-type Ge, orthorhombic α-S (Fddd, 32 atoms in the primitive cell) and trigonal Se, all at their experimental lattice parameters [31–33] (COD entries 9008468, 9008484, 9008567, 9011362 and 9012501 [34]). A negative ΔH_f does not guarantee stability, because the compound may decompose into other compounds. We therefore also computed the reaction energy against the competing phases Cu_2GeS_3 (Cc), Cu_2GeSe_3 (Imm2), SrS and SrSe (rock salt):

$$\Delta H_r(x) = \frac{1}{8}\left[E(x) - \min_{\{n_i\}} \sum_i n_i E_i\right], \qquad (3)$$

where the minimum runs over all mixtures of these phases with the composition of $Cu_2SrGeS_{4-x}Se_x$. A negative ΔH_r means that the compound lies below this decomposition limit. The chemical potentials cancel in ΔH_r, which is therefore insensitive to the elemental references. We optimized the volumes of SrS and SrSe, starting from their experimental rock-salt cells [31] (COD 9008728 and 9008729), and took Cu_2GeS_3 and Cu_2GeSe_3 at their Materials Project PBE geometries [19]. The mixing enthalpy of the alloys, with y = x/4, is

$$\Delta H_{\mathrm{mix}}(y) = \frac{1}{8}[E(y) - (1-y)\,E(0) - y\,E(1)], \qquad (4)$$

and we compared it with the ideal configurational entropy of the anion sublattice, which holds half of the atoms:

$$S_{\mathrm{id}}(y) = -\frac{k_B}{2}[y\ln y + (1-y)\ln(1-y)], \qquad T^* = \frac{\Delta H_{\mathrm{mix}}}{S_{\mathrm{id}}}. \qquad (5)$$

Finally, the structural energy $\Delta E_{str} = E(P3_2) - E(Ama2)$, per atom, compares the trigonal and orthorhombic polymorphs at x = 0 and x = 4. All energies in this section are PBE energies without U, which keeps the metallic Cu reference and the compounds at the same level of theory [35].

2.5. Optical properties

We computed the linear optical response in the independent-particle approximation with the OPTIC module [36], without local-field or excitonic effects. The imaginary part of the dielectric tensor is :

$$\varepsilon_2^{\alpha\beta}(\omega) = \frac{4\pi^2 e^2}{m^2\omega^2}\sum_{c,v}\int_{\mathrm{BZ}} \frac{2\,d^3k}{(2\pi)^3}\,\langle c\mathrm{k}|p_\alpha|v\mathrm{k}\rangle\langle v\mathrm{k}|p_\beta|c\mathrm{k}\rangle\,\delta(E_{c\mathbf{k}} - E_{v\mathbf{k}} - \hbar\omega), \qquad (6)$$

and the real part $\varepsilon_1(\omega)$ follows from the Kramers–Kronig relation. The trigonal symmetry leaves two independent components, xx (= yy, light polarized in the basal plane) and zz (along c). The absorption coefficient, refractive index, reflectivity and energy-loss function follow from ε_1 and ε_2:

$$\alpha(\omega) = \frac{\sqrt{2}\,\omega}{c}\left(\sqrt{\varepsilon_1^2 + \varepsilon_2^2} - \varepsilon_1\right)^{1/2}, \qquad n(\omega) = \left(\frac{\sqrt{\varepsilon_1^2 + \varepsilon_2^2} + \varepsilon_1}{2}\right)^{1/2}, \qquad (7)$$

$$R(\omega) = \frac{(n-1)^2 + k^2}{(n+1)^2 + k^2}, \qquad L(\omega) = \frac{\varepsilon_2}{\varepsilon_1^2 + \varepsilon_2^2}, \qquad (8)$$

where k is the extinction coefficient. The optical spectra were computed on a denser mesh of 3000 k-points in the full zone.

2.6. Detailed-balance efficiency limit

We evaluated the Shockley–Queisser limit [4] for each computed gap E_g. We assumed that the cell absorbs every photon above E_g and loses carriers only by radiative recombination, at T = 300 K under the AM1.5G spectrum (ASTM G173-03, 1000 W m^{-2}) [37], taken from the pvlib library [38]:

$$J_{sc} = q\int_{E_g}^{\infty} \Phi_{\mathrm{AM1.5G}}(E)\,dE, \qquad J_0 = \frac{2\pi q}{h^3c^2}\int_{E_g}^{\infty}\frac{E^2\,dE}{\exp(E/k_BT) - 1}, \qquad (9)$$

$$J(V) = J_{sc} - J_0\left[\exp\left(\frac{qV}{k_BT}\right) - 1\right], \qquad \eta = \frac{\max_V [J(V)\,V]}{P_{\mathrm{in}}}. \qquad (10)$$

3. Crystal structure and thermodynamic stability

3.1. Lattice parameters

Cu_2SrGeS_4 crystallizes in the trigonal space group $P3_2$ (No. 145) with three formula units per cell (Fig. 1) [15]. In this structure Cu and Ge occupy tetrahedral sites, while Sr is eightfold coordinated by S [9,15]. In our optimized structure, the CuS_4 and GeS_4 tetrahedra share corners only (Cu–S = 2.29–2.34 Å, Ge–S = 2.25–2.26 Å), and each S atom bonds to two Cu, one Ge and two Sr atoms (Sr–S = 3.09–3.23 Å). Our PBE optimization gives a = 6.1931 Å, c = 15.1129 Å and V = 501.98 $Å^3$ (Table 1). The lattice parameter a is in good agreement with the experimental value of 6.1431 Å [15], with a deviation of +0.81%. The c parameter is underestimated by 1.11%, so that the volume error nearly cancels (+0.50%) and c/a is 1.9% smaller than measured (2.440 vs 2.488). The usual PBE overestimation of bond lengths accounts for a and V, but not for the contraction along c.

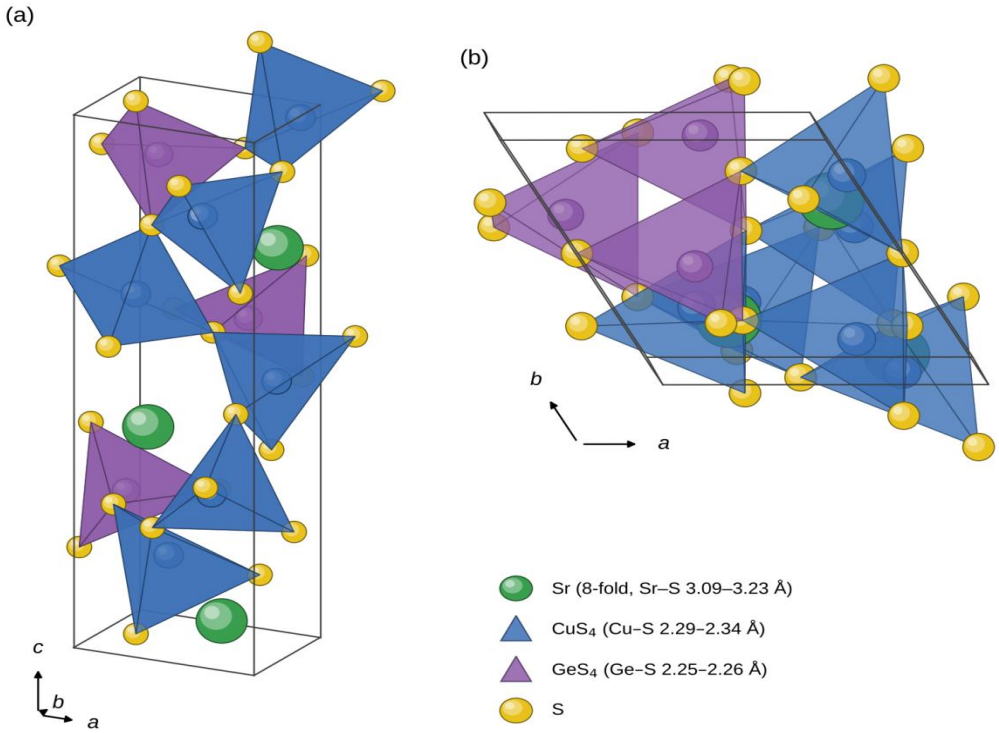

Fig.1 PBE-optimized crystal structure of trigonal Cu_2SrGeS_4 (space group $P3_2$, Z = 3): (a) side view with the c axis vertical and (b) view along c. The CuS_4 (blue) and GeS_4 (purple) tetrahedra share corners only, and each Sr atom (green) is coordinated by eight S atoms (yellow). The bond-length ranges are given in the legend.

Table 1: PBE lattice parameters of $P3_2$ $Cu_2SrGeS_{4-x}Se_x$. δV is the deviation of the volume from a linear interpolation between x = 0 and x = 4.

x	a (Å)	c (Å)	c/a	V ($Å^3$)	δV (%)
0	6.1931	15.1129	2.440	501.98	0
1	6.2793	15.5897	2.483	532.34	+1.6
2	6.3525	15.8379	2.493	553.49	+1.4
3	6.4416	15.9879	2.482	574.52	+1.1
4	6.4387	16.4359	2.553	590.09	0
0, exp. [15]	6.1431	15.2832	2.488	499.48	–

The cell expands with Se content, as expected from the larger ionic radius of Se^{2-} (1.98 Å, against 1.84 Å for S^{2-}) [39]. The expansion is anisotropic. From x = 0 to x = 4, a grows by 4.0%, c by 8.8% and V by 17.6% (Fig. 4a). The c/a ratio rises from 2.440 to 2.553, but not monotonically: it stays near 2.48–2.49 for x = 1–3, and a is marginally larger at x = 3 than at x = 4. The volume also deviates from Vegard's law [40], by +1.1 to +1.6% for the intermediate compositions. Both features reflect the ordered occupation of specific anion sites. Each of the four inequivalent anion sites bonds to Sr and to the Cu/Ge framework with a different geometry, so the axis that expands most depends on which sites hold Se.

3.2. Formation enthalpy

All compositions have a large negative formation enthalpy (Table 2, Fig. 2a). ΔH_f rises linearly from −0.815 eV/atom at x = 0 to −0.698 eV/atom at x = 4, by 29 meV/atom per unit of x. This trend follows the lower electronegativity of Se, which makes the metal–Se bonds less ionic and weaker than the metal–S bonds. For the parent, the Materials Project lists an uncorrected PBE value of −0.793 eV/atom [19]. For the orthorhombic selenide, it lists −0.694 eV/atom. Our values are lower by 22 and 16 meV/atom, respectively. Over the five phases for which both data sets exist, the offset has the same sign and lies between 16 and 47 meV/atom. It most likely comes from the elemental references, which we took at their experimental geometries, and it cancels in the reaction energies discussed next.

Table 2: Formation enthalpy ΔH_f, reaction energy ΔH_r against the competing phases, mixing enthalpy ΔH_{mix}, and the temperature $T^* = \Delta H_{mix}/S_{id}$ above which configurational entropy outweighs the mixing enthalpy.

x	Structure	ΔH_f (eV/atom)	ΔH_r (meV/atom)	ΔH_{mix} (meV/atom)	T* (K)
0	$P3_2$	−0.815	−14.5	–	–
1	$P3_2$	−0.785	−4.6	+1.2	48
2	$P3_2$	−0.756	+3.5	+0.6	21
3	$P3_2$	−0.727	+12.6	+0.9	39
4	$P3_2$	−0.698	+16.3	–	–
4	Ama2	−0.710	+4.6	–	–

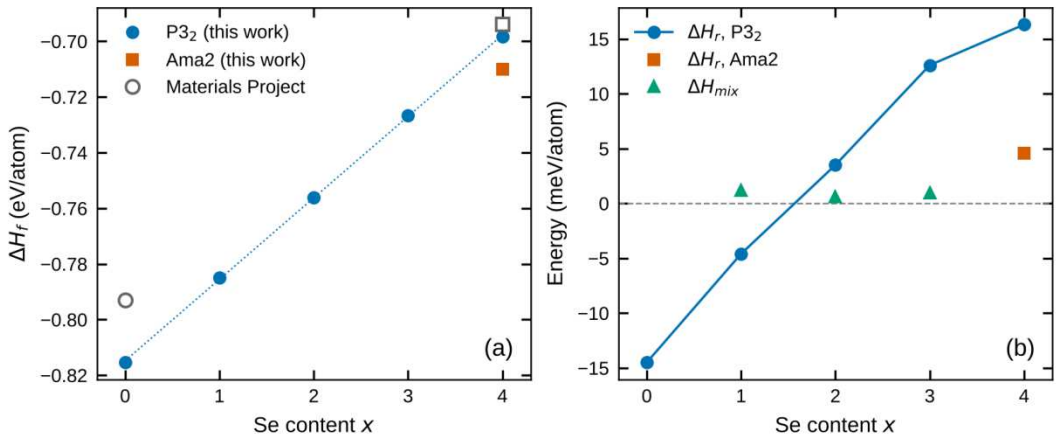

Fig.2 (a) Formation enthalpy ΔH_f of $Cu_2SrGeS_{4-x}Se_x$ in the $P3_2$ structure (circles) and of $Cu_2SrGeSe_4$ in the Ama2 structure (square), compared with the uncorrected PBE values of the Materials Project (open symbols) [19]; the dotted line is a linear fit. (b) Reaction energy ΔH_r against the competing phases Cu_2GeS_3, Cu_2GeSe_3, SrS and SrSe, and mixing enthalpy ΔH_{mix} of the ordered alloys. The dashed line marks the decomposition limit.

3.3. Stability against competing phases

A negative ΔH_f only shows that the compound is stable against its elements. The relevant test is the reaction energy against the competing binary and ternary chalcogenides. As shown in Fig. 2b, the parent lies 14.5 meV/atom below the decomposition limit Cu_2GeS_3 + SrS. Se substitution raises ΔH_r by 8–10 meV/atom per unit of x up to x = 3, and by a further 3.7 meV/atom to +16.3 meV/atom at x = 4, where the competing phases are Cu_2GeSe_3 + SrSe. The sign change occurs near x ≈ 1.6. For the intermediate compositions, the lowest-energy products always place S on Sr and Se in the Cu–Ge chalcogenide. The exchange SrSe + ⅓ Cu_2GeS_3 → SrS + ⅓ Cu_2GeSe_3 releases 32 meV per exchanged anion. This preference is consistent with the hard–soft acid–base principle [41]: the hard Sr^{2+} cation favours the harder S^{2-} anion, whereas the soft Cu^+ favours Se^{2-}. In the quaternary, Se cannot avoid bonding to Sr, and this cost grows with x.

The experimentally known Ama2 selenide lies 4.6 meV/atom above the same limit in our calculation, close to the 7 meV/atom given by the Materials Project [19]. Synthesized compounds computed a few meV/atom above the hull are common, and most known metastable inorganic compounds lie within a few tens

of meV/atom of it [42]. The trigonal members with $x \geq 2$, at 3.5–16.3 meV/atom above the limit, are therefore metastable and fall within this range. The driving force, however, favours the S-rich side. Configurational entropy could shift the boundary: for an ideal anion solution, $T \cdot S_{id}$ reaches 7–9 meV/atom at 300 K, of the same order as ΔH_r near $x = 2$. A quantitative statement would require the entropy of the competing $Cu_2Ge(S,Se)_3$ solid solutions as well. Two approximations limit the accuracy of these numbers. We computed one ordered configuration per composition, and we took the ternary phases at their Materials Project PBE geometries without further relaxation. Relaxing SrS and SrSe changed ΔH_r by less than 1 meV/atom.

3.4. Mixing enthalpy

The mixing enthalpies of the ordered alloys are small and positive, between +0.6 and +1.2 meV/atom (Table 2). The ideal configurational entropy outweighs them above $T^* = 21–48$ K. At any practical growth temperature, the anion sublattice therefore behaves as a nearly ideal solution. The Se-rich members lose their stability through decomposition into the binary and ternary chalcogenides of Section 3.3, and S/Se demixing within the trigonal lattice does not contribute.

3.5. Trigonal versus orthorhombic polymorph

At $x = 0$, the $P3_2$ structure is lower than the Ama2 structure by 11.3 meV/atom. Our Ama2 cell for the sulfide was obtained by scaling the selenide cell and was not relaxed, so this value is an upper bound on the advantage of $P3_2$. At $x = 4$, the order is reversed: Ama2 is lower by 11.8 meV/atom. Here the $P3_2$ cell is fully relaxed and the Ama2 cell is not, so this value is a lower bound on the advantage of Ama2. Both results agree with experiment, which reports $P3_2$ for the sulfide [15] and Ama2 for the selenide [18,19]. A linear interpolation places the crossover near $x \approx 2$, close to the composition at which the trigonal phase crosses the decomposition limit. Consequently, the electronic and optical results of Sections 4 and 5 for $x \geq 2$ describe metastable trigonal phases. They are not ground states, although non-equilibrium thin-film growth might stabilize them.

4. Electronic structure

4.1. Band structure and band gap

Fig. 3 shows the band structures of the series. For all compositions, the conduction-band minimum (CBM) lies at Γ. The valence-band maximum (VBM) lies off Γ, on the Γ–A line for the parent, and 9–17 meV above the Γ-point valence state (Table 3). The gap is therefore quasi-direct. Since this offset is smaller than k_BT at room temperature (26 meV), the direct Γ→Γ transition sets the absorption edge. For the parent, the fundamental gap is 1.361 eV and the direct gap at Γ is 1.373 eV. A second conduction valley at K lies 0.05 eV above the CBM in the parent.

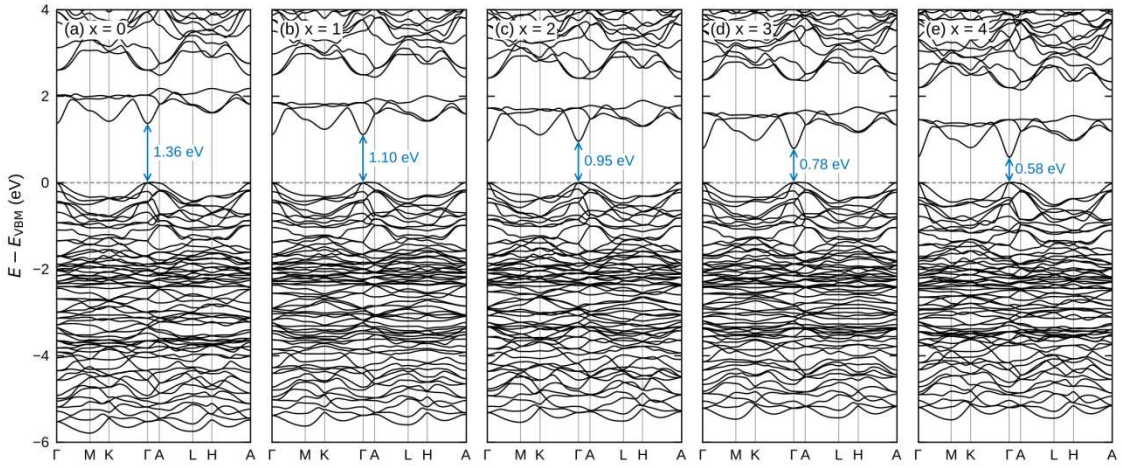

Fig.3 GGA+U band structures of $Cu_2SrGeS_{4-x}Se_x$ along Γ–M–K–Γ–A–L–H–A: (a) x = 0, (b) x = 1, (c) x = 2, (d) x = 3 and (e) x = 4. Energies are referred to the VBM; the arrows mark the fundamental gap.

Our PBE calculation for the parent gives a quasi-direct gap of 1.04 eV with the same band-edge positions. The Hubbard term thus opens the gap by 0.32 eV. It shifts the Cu 3d band centroid from −1.93 to −2.32 eV and reduces the Cu 3d weight of the VBM state (inside the spheres) from 0.47 to 0.38, while the S 3p weight rises from 0.23 to 0.27. The larger separation between the Cu 3d and S 3p states weakens their repulsion, which pushes the VBM up in semilocal calculations [5,27]. Consequently, the VBM moves down and the gap opens. The character of the CBM does not change with U. The measured optical gap of the parent is 2.8 eV [16], about twice our value. With this moderate U, GGA+U removes only part of the semilocal gap error. We therefore use the computed gaps to compare compositions rather than as quantitative predictions.

As shown in Fig. 4b, the gap decreases with increasing Se content, from 1.36 eV at x = 0 to 0.58 eV at x = 4, i.e. by about 0.19 eV per unit of x. A quadratic fit with fixed end points gives a bowing parameter b = 0.12 eV. The x = 1 point lies 0.04 eV below the fit and the x = 3 point 0.03 eV above it. These deviations are of the order expected from the use of a single ordered configuration per composition. The small bowing is consistent with the similar chemistry of S and Se and with the nearly ideal mixing found in Section 3.4.

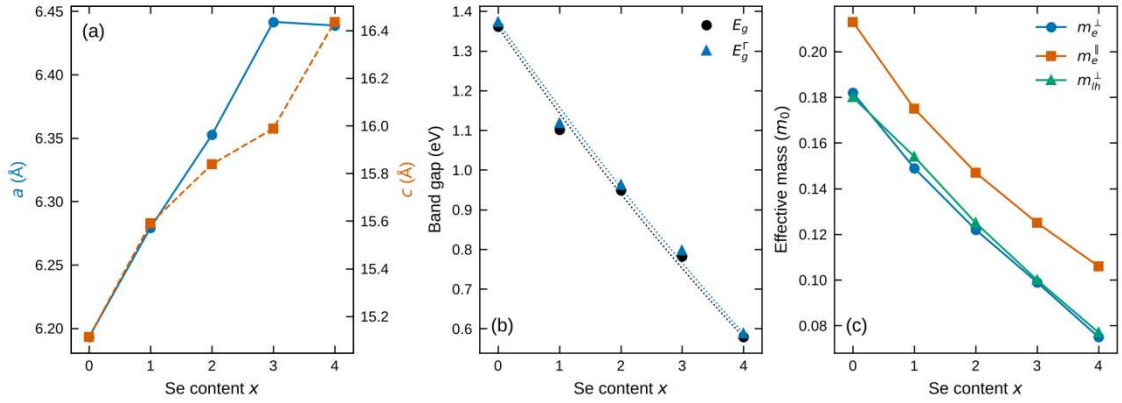

Fig.4 Composition dependence of (a) the lattice parameters a and c, (b) the fundamental gap E_g and the direct gap at Γ, E_g^Γ, with quadratic fits (dotted lines), and (c) the effective masses of the electrons ($m_{e\perp}$, $m_{e\parallel}$) and of the light holes ($m_{lh\perp}$).

4.2. Densities of states and band-gap character

Fig. 5 shows the total and projected densities of states. The upper valence band is formed by Cu 3d states hybridized with the anion p states. The VBM is an antibonding Cu 3d–S 3p state: in the parent, its weights inside the spheres are 0.38 for Cu 3d and 0.27 for S 3p. The CBM is an antibonding state built from Ge 4s and S 3s/3p orbitals, with a Cu 4s contribution (Ge 4s 0.12, S 3s 0.18, S 3p 0.13, Cu 4s 0.10) and no Cu 3d weight. Sr contributes little to either edge (≤ 0.03). Its states lie deep in the valence band and high in the conduction band, so Sr acts as an electron donor and a structural spacer. The lowest conduction band is separated from the higher conduction states, and its width grows from 0.81 eV at x = 0 to 0.95 eV at x = 4.

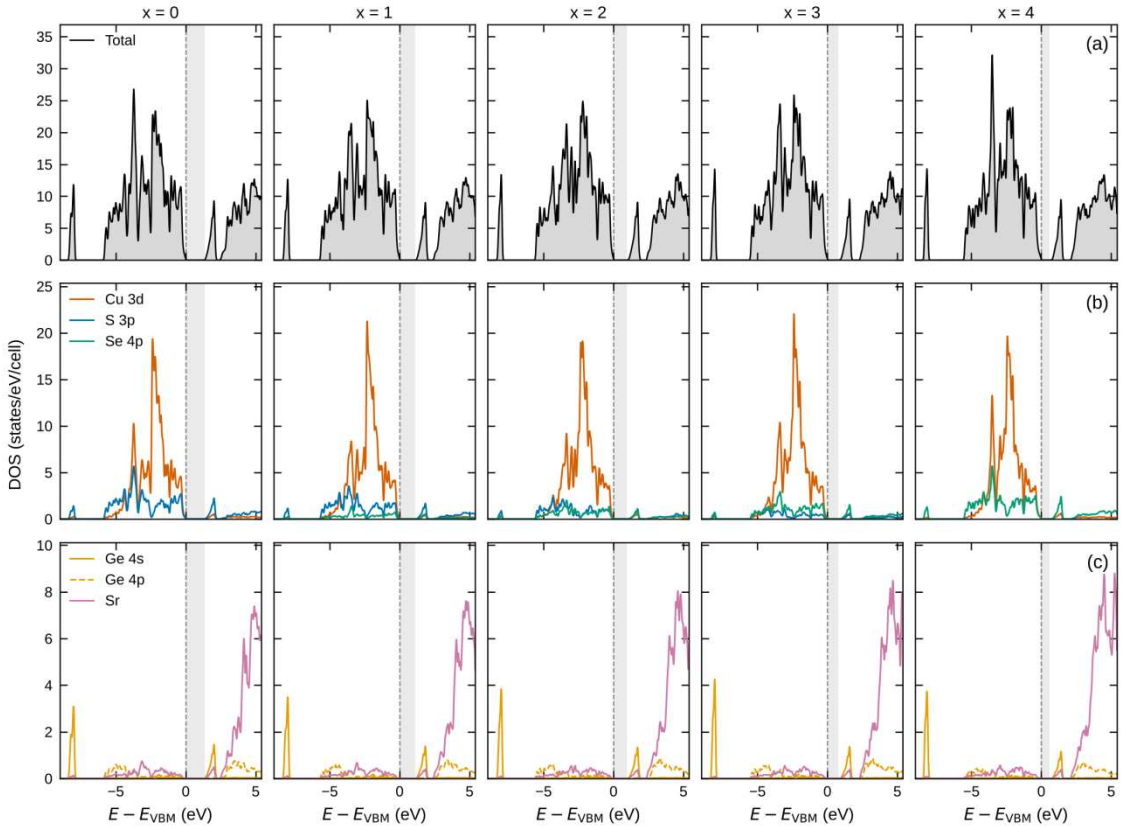

Fig.5 (a) Total DOS and partial DOS of (b) Cu 3d, S 3p and Se 4p and (c) Ge 4s, Ge 4p and Sr states in $Cu_2SrGeS_{4-x}Se_x$ (GGA+U, one spin channel). Energies are referred to the VBM, and the grey band marks the gap. The partial DOS are muffin-tin projections summed over equivalent sites.

In the mixed compositions, the Se 4p share of the anion p weight at the VBM is 28, 56 and 77% for x = 1, 2 and 3. These values exceed the nominal Se fractions of 25, 50 and 75% by 2–6 percentage points. The Se 4p states lie higher than the S 3p states, because Se is less electronegative, and they therefore dominate the top of the valence band. This raises the VBM with x. At the same time, the cell expansion lengthens the Ge–anion bonds, which lowers the anti bonding CBM and broadens the lowest conduction band. Both effects narrow the gap. Our calculations give no absolute band positions, so they do not separate the shifts of the two edges. An alignment through a common reference, such as a core level or a slab calculation, would settle this point.

4.3. Effective masses and effective densities of states

Table 2: Band-gap parameters of $Cu_2SrGeS_{4-x}Se_x$ (GGA+U): fundamental gap E_g, direct gap at Γ E_g^{Γ}, offset ΔE_v (meV) of the VBM above the Γ valence state, crystal-field splitting at Γ Δ_{CF}, effective masses (in m_0) of the electrons, the heavy holes (top valence band) and the light holes (second valence band), and effective densities of states at 300 K.

x	E_g (eV)	E_g^{Γ} (eV)	ΔE_v	Δ_{CF} (eV)	$m_{e\perp}$	$m_{e\parallel}$	$m_{hh\perp}$	$m_{hh\parallel}$	$m_{lh\perp}$	N_c (10^{18} cm^{-3})	N_v (10^{19} cm^{-3})
0	1.361	1.373	12	0.200	0.182	0.213	0.96	1.76	0.180	2.11	3.74
1	1.101	1.118	17	0.201	0.149	0.175	1.06	2.01	0.154	1.57	4.28
2	0.949	0.963	14	0.142	0.122	0.147	0.99	2.21	0.125	1.18	4.11
3	0.782	0.797	15	0.184	0.099	0.125	0.88	1.89	0.100	0.88	3.35
4	0.579	0.588	9	0.344	0.075	0.106	1.46	1.31	0.077	0.61	4.39

The conduction electrons are light and weakly anisotropic (Table 3, Fig. 4c). Their in-plane mass decreases from 0.182 m_0 at x = 0 to 0.075 m_0 at x = 4, and the ratio $m_{e\parallel}/m_{e\perp}$ grows from 1.17 to 1.41. The electron mass scales with the gap, as expected from k·p coupling across the gap. A two-band Kane estimate, $m_0/m_{e\perp} = 1 + E_P/E_g$, gives $E_P \approx 6$–7 eV for the whole series. These electron masses are comparable to those reported for kesterite Cu_2ZnSnS_4 [43]. The valence band is more complex. The top band is heavy, 0.9–1.5 m_0 in the plane and 1.3–2.2 m_0 along c. The second band is

light in the plane, and its mass follows the electron mass within 3% (0.180 against 0.182 m_0 at x = 0). This mirror relation indicates that the in-plane k·p coupling of the CBM runs mainly through this second band.

The effective density of states of the conduction band is small and falls from 2.1×10^{18} to 6.1×10^{17} cm^{-3} across the series. The valence band, dominated by the heavy top band, gives $N_v = (3.4–4.4) \times 10^{19}$ cm^{-3}, an order of magnitude larger. Moderate n-type doping would therefore make the Se-rich members degenerate. For a p-type absorber, the light minority electrons favour carrier collection, provided that defects do not limit their lifetime.

5. Optical properties

5.1. Dielectric function and absorption edge

Figs. 6 and 7 show the optical spectra for light polarized in the basal plane (xx) and along c (zz), and Table 4 collects the main optical parameters.

Table 4 : Optical parameters of $Cu_2SrGeS_{4-x}Se_x$ (GGA+U, independent-particle approximation) for xx and zz polarization: onset of ε_2, position of the first ε_2 peak, static dielectric constant, static refractive index, static reflectivity (xx), photon energy at which α reaches 10^5 cm^{-1}, and main peak of the energy-loss function (xx).

x	Onset xx / zz (eV)	First ε_2 peak xx / zz (eV)	$\varepsilon_1(0)$ xx / zz	n(0) xx / zz	R(0) (%)	E(α = 10^5 cm^{-1}) xx / zz (eV)	L peak (eV)
0	1.41 / 1.61	2.30 / 2.46	7.92 / 7.68	2.81 / 2.77	22.6	2.03 / 2.14	17.29
1	1.16 / 1.35	2.08 / 2.24	8.41 / 8.36	2.90 / 2.89	23.7	1.81 / 1.89	17.16
2	1.01 / 1.13	1.95 / 2.11	8.94 / 9.01	2.99 / 3.00	24.9	1.70 / 1.73	16.99
3	0.83 / 1.01	1.84 / 2.00	9.56 / 9.41	3.09 / 3.07	26.1	1.59 / 1.67	16.72
4	0.63 / 0.84	1.73 / 1.92	10.46 / 10.15	3.23 / 3.19	27.8	1.46 / 1.59	16.50

For xx polarization, the onset of ε_2 moves from 1.41 eV in the parent to 0.63 eV at x = 4. These onsets lie 0.03–0.04 eV above the direct gap at Γ (Table 3), so the absorption edge is set by the Γ→Γ transition and follows the gap across the series. The zz onset is delayed by 0.19, 0.19, 0.12, 0.18 and 0.22 eV for x = 0–4. For $x \leq 3$, this delay matches the crystal-field splitting at Γ within 0.02 eV. In the trigonal point group 3, the two highest valence states at Γ are p_x,p_y-like (E), while the p_z-like (A) state lies Δ_{CF} lower. Transitions from the E states to the s-like CBM couple only to light polarized in the basal plane. The first zz transition therefore starts from the A state, Δ_{CF} higher in energy. At x = 4, the delay (0.22 eV) is smaller than Δ_{CF} (0.34 eV), which suggests that the ordering or character of the valence states below the VBM changes at this composition.

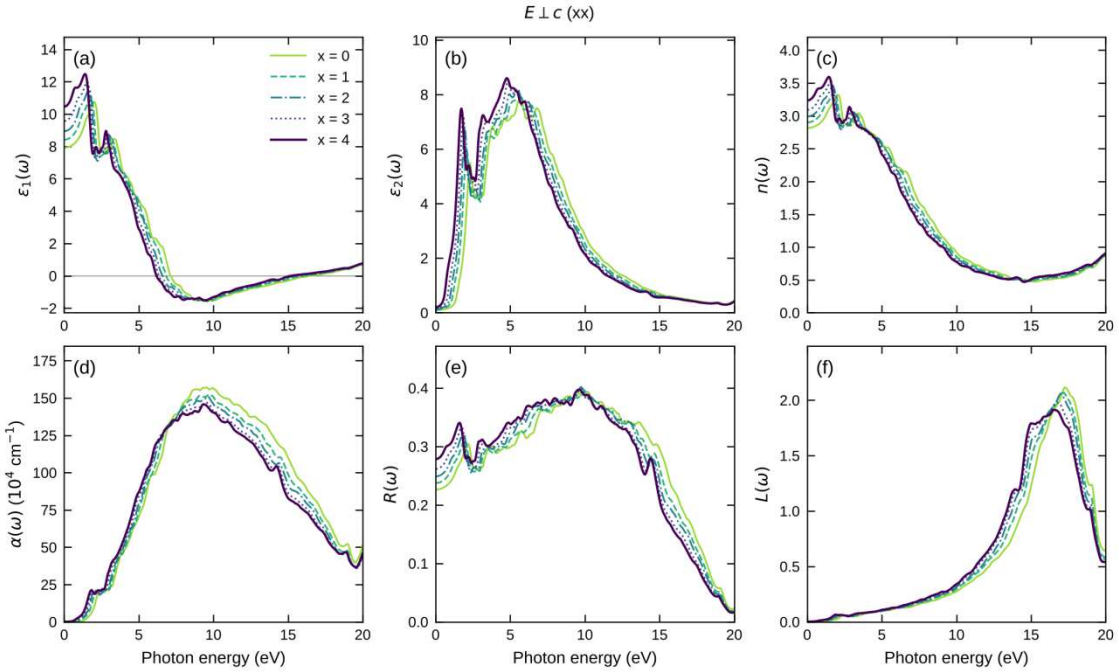

Fig.6 Optical spectra of $Cu_2SrGeS_{4-x}Se_x$ for light polarized in the basal plane (xx): (a) $\varepsilon_1(\omega)$, (b) $\varepsilon_2(\omega)$, (c) refractive index $n(\omega)$, (d) absorption coefficient $\alpha(\omega)$, (e) reflectivity $R(\omega)$ and (f) energy-loss function $L(\omega)$.

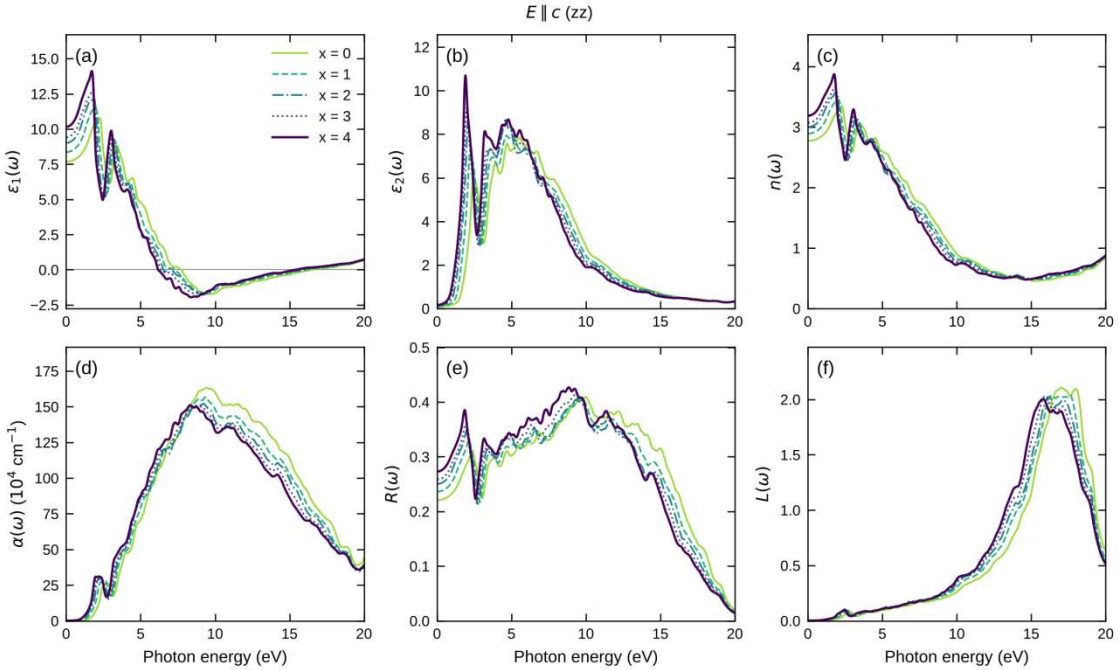

Fig.7 Same as Fig. 6 for light polarized along the c axis (zz).

The first ε_2 peak red-shifts with x, from 2.30 to 1.73 eV (xx) and from 2.46 to 1.92 eV (zz). It arises from transitions into the isolated lowest conduction band. The main ε_2 maximum, near 5.7 eV in the parent and 4.8 eV at x = 4 (xx), involves the higher conduction states. Above the edge the optical anisotropy is weak: the xx and zz spectra differ mainly by the onset shift and by the relative weights of the first peaks.

5.2. Refractive index, reflectivity and absorption

The static dielectric constant increases with Se content, from 7.92 to 10.46 (xx) and from 7.68 to 10.15 (zz). This inverse relation with the gap is the expected behaviour of semiconductors, since a smaller gap reduces the energy denominators of the interband polarizability. The static refractive index follows $n(0) = \varepsilon(0)^{\frac{1}{2}}$, from 2.81 to 3.23 (xx), and the static reflectivity rises from 22.6 to 27.8%. These values are moderate. A device would need an antireflection coating, as for other chalcogenide absorbers.

As shown in Figs. 6d and 7d, the absorption coefficient exceeds 10^5 cm^{-1} above 2.03 eV in the parent and above 1.46 eV at x = 4 (xx). A coefficient of 10^5 cm^{-1} corresponds to an absorption length of 100 nm, so a film of about 1 μm absorbs most of the light above these energies. Between the onset and this threshold, however, α rises over 0.6–0.8 eV. This gradual rise reflects the modest joint density of states of the single isolated conduction band. It will reduce the photocurrent of thin films below the step-function limit of Section 6. At higher energies, α reaches about 1.5×10^6 cm^{-1} near 9.5 eV for all compositions.

5.3. Energy-loss function

The energy-loss function L(ω) shows a main peak at 17.29 eV in the parent for xx polarization, which shifts to 16.50 eV at x = 4 (Fig. 6f). The zz spectrum shows a doublet whose lower component moves from 17.02 to 15.80 eV (Fig. 7f). We assign these peaks to the bulk plasmon of the valence electrons. Their red shift with x follows the lower valence-electron density of the expanded cell (V +17.6%).

The spectra were computed in the independent-particle approximation. Excitonic effects would shift spectral weight towards the edge [44], and the absolute energies inherit the gap error of Section 4.1. The trends with x, the polarization dependence of the edge and the anisotropy of the static constants are less sensitive to these approximations.

6. Relevance for photovoltaics

Table 5 gives the detailed-balance limits obtained from the computed fundamental gaps (Section 2.6).

Table 5 : Shockley–Queisser limits (AM1.5G, 300 K) evaluated at the GGA+U gaps E_g: short-circuit current density J_{sc}, open-circuit voltage V_{oc}, fill factor FF and efficiency η.

x	E_g (eV)	J_{sc} (mA cm^{-2})	V_{oc} (V)	FF	η (%)
0	1.361	34.3	1.10	0.891	33.6
1	1.101	44.2	0.86	0.868	32.9
2	0.949	51.0	0.72	0.849	31.1
3	0.782	55.6	0.56	0.819	25.6
4	0.579	63.3	0.38	0.761	18.2

The computed gap of the parent, 1.36 eV, lies close to the single-junction optimum, and its limiting efficiency (33.6%) is within 0.1 percentage point of the maximum of the AM1.5G curve, 33.7% [45]. With increasing Se content, the gain in current no longer compensates the loss in voltage. The limit stays above 31% up to x = 2 and then falls to 18.2% at x = 4. The quasi-direct character of the gap carries no penalty here, because the VBM offset ($\leq$ 17 meV) is below k_BT.

Combined with Section 3, these limits single out the S-rich part of the series. The trigonal phase is favoured against decomposition only for $x \lesssim 1.6$, and over this range the computed gaps (1.36 to about 1.0 eV) give limits of 32–34%. The compositions that remain thermodynamically accessible are thus also those with the most favourable gaps in our calculation. Two points qualify this statement. First, our GGA+U calculation does not fix the absolute gap scale (Section 4.1). A larger true gap would move the composition of optimum gap towards higher x, where the trigonal phase is metastable. Second, the SQ limit assumes a step-like absorptance, whereas our absorption edges rise over 0.6–0.8 eV before reaching 10^5 cm^{-1} (Section 5.2). A thickness-dependent metric such as the spectroscopic limited maximum efficiency [46], evaluated with the computed α(ω), would quantify this loss. Non-radiative recombination through defects, which the SQ limit ignores, remains the decisive open question for this family [7,9,10].

7. Conclusions

We have studied the trigonal series $Cu_2SrGeS_{4-x}Se_x$ (x = 0–4) with the FP-LAPW+lo method, using PBE for structures and energetics and GGA+U (U = 3.95 eV on Cu 3d) for the electronic and optical properties. The PBE lattice parameters of the parent agree with experiment within 1.1%, and full substitution expands the cell by 17.6%, preferentially along c. All members have negative formation enthalpies, but the trigonal structure is stable against Cu_2GeS_3, Cu_2GeSe_3, SrS and SrSe only for $x \lesssim 1.6$. The reaction energy rises from −14.5 to +16.3 meV/atom across the series, driven by the preference of Sr for S and of the Cu–Ge framework for Se, whereas the mixing enthalpy never exceeds 1.2 meV/atom. The orthorhombic Ama2 polymorph becomes favoured near $x \approx 2$, in agreement with the known structures of both end members. The gap is quasi-direct for all compositions, with the CBM at Γ and the VBM within 17 meV of the Γ state. It narrows from 1.36 to 0.58 eV with a bowing of 0.12 eV, through the rising Se 4p contribution to the VBM and the expansion of the cell. Conduction electrons are light (0.08–0.21 m_0), the zz absorption edge is delayed by the crystal-field splitting of the valence band, and the absorption coefficient exceeds 10^5 cm^{-1} above 1.46–2.03 eV. Within the detailed-balance limit, the S-rich compositions that remain thermodynamically favoured also have the best computed gaps, with limits of 32–34%. These results identify $Cu_2SrGeS_{4-x}Se_x$ with $x \lesssim 1.6$ as the most promising part of the series. Measurements of the optical gap and of phase stability across the series are now needed to fix the absolute gap scale and to test the predicted stability boundary.

Acknowledgments

We would like to thank Professor Boukortt Abdelkader of Laboratory development, physicomechanical and metallurgical characterization of Materials (ECP3M), Abdelhamid Ibn Badis University for her support during of this study.

Statements and Declarations

The authors declare that they have no known competing personal relationships or financial interests that could appear to influence the work reported in this paper.

Funding Declaration

This research received no external funding.

References

[1] Babayigit A, et al. (2016) Toxicity of organometal halide perovskite solar cells. Nature Materials 15:247–251. doi.org/10.1038/nmat4572.

[2] Candelise C, et al. (2012) Implications for CdTe and CIGS technologies production costs of indium and tellurium scarcity. Progress in Photovoltaics: Research and Applications 20:816–831. doi.org/10.1002/pip.2216.

[3] Frenzel M, et al. (2016) On the current and future availability of gallium. Resources Policy 47:38–50. doi.org/10.1016/j.resourpol.2015.11.005.

[4] Shockley W, Queisser HJ (1961) Detailed balance limit of efficiency of p–n junction solar cells. Journal of Applied Physics 32:510–519. doi.org/10.1063/1.1736034.

[5] Botti S, Kammerlander D, Marques MAL (2011) Band structures of Cu_2ZnSnS_4 and Cu2ZnSnSe4 from many-body methods. Applied Physics Letters 98:241915. doi.org/10.1063/1.3600060.

[6] Zhang Y, et al. (2011) Comparative study of structural and electronic properties of Cu-based multinary semiconductors. Physical Review B 84:075127. doi.org/10.11 03/PhysRevB.84.075127.

[7] Chen S, et al. (2010) Defect physics of the kesterite thin-film solar cell absorber Cu2ZnSnS4. Applied Physics Letters 96:021902. doi.org/10.1063/1.3275796.

[8] Chen S, et al. (2010) Intrinsic point defects and complexes in the quaternary kesterite semiconductor Cu_2ZnSnS_4. Physical Review B 81:245204. doi.org/10.1103/Phys RevB.81.245204.

[9] Hong F, Lin W, Meng W, Yan Y (2016) Trigonal Cu_2-II-Sn-VI_4 (II = Ba, Sr and VI = S, Se) quaternary compounds for earth-abundant photovoltaics. Physical Chemistry Chemical Physics 18:4828–4834. doi.org/10.1039/C5CP06977G.

[10] Zhu T, et al. (2017) I_2–II–IV–VI_4 (I = Cu, Ag; II = Sr, Ba; IV = Ge, Sn; VI = S, Se): chalcogenides for thin-film photovoltaics. Chemistry of Materials 29:7868–7879. doi.org/10.1021/acs.chemmater.7b02638.

[11] Shin D, et al. (2017) Earth-abundant chalcogenide photovoltaic devices with over 5% efficiency based on a $Cu_2BaSn(S,Se)_4$ absorber. Advanced Materials 29:1606945. doi.org/10.1002/adma.201606945.

[12] Crovetto A, et al. (2020) Experimental and first-principles spectroscopy of Cu_2SrSnS_4 and Cu_2BaSnS_4 photoabsorbers. ACS Applied Materials & Interfaces 12:50446–50454. doi.org/10.1021/acsami.0c14578.

[13] Dzade NY (2021) First-principles insights into the electronic structure, optical and band alignment properties of earth-abundant Cu_2SrSnS_4 solar absorber. Scientific Reports 11:4755. doi.org/10.1038/s41598-021-84037-8.

[14] Wessler GC, et al. (2018) Band gap tailoring and structure–composition relationship within the alloyed semiconductor $Cu_2BaGe_{1-x}Sn_xSe_4$. Chemistry of Materials 30:6566–6574. doi.org/10.1021/acs.chemmater.8b03380.

[15] Teske ChrL (1979) Über die Darstellung und röntgenographische Untersuchung von Cu_2SrGeS_4 und Cu_2BaGeS_4 (On the preparation and X-ray investigation of Cu_2SrGeS_4 and Cu_2BaGeS_4). Zeitschrift für Naturforschung B 34:386–389. doi.org/10.1515/znb-1979-0306.

[16] Llanos J, et al. (2003) Physical and optical properties of the quaternary sulfides $SrCu_2MS_4$ and $EuCu_2MS_4$ (M = Ge and Sn). Journal of Solid State Chemistry 173:78–82. doi.org/10.1016/S0022-4596(03)00093-8.

[17] Abubakr M, et al. (2023) First principles quantum analysis of structural, electronic, optical and thermoelectric properties of XCu_2GeQ_4 (X = Ba, Sr and Q = S, Se) for energy applications. Optical and Quantum Electronics 55:849. doi.org/10.1007/s11082-023-05136-6.

[18] Kuo JJ, et al. (2019) Origins of ultralow thermal conductivity in 1-2-1-4 quaternary selenides. Journal of Materials Chemistry A 7:2589–2596. doi.org/10.1039/C8TA09660K.
[19] Jain A, et al. (2013) Commentary: The Materials Project: A materials genome approach to accelerating materials innovation. APL Materials 1:011002. doi.org/10.1063/1.4812323.
[20] Gunatilleke WDCB, et al. (2020) Thermal properties of $BaCu_2SnQ_4$ (Q = S, Se) quaternary chalcogenides. Applied Physics Letters 117:092101. doi.org/10.1063/5.0013406.
[21] Chen S, et al. (2011) Compositional dependence of structural and electronic properties of $Cu_2ZnSn(S,Se)_4$ alloys for thin film solar cells. Physical Review B 83:125201. doi.org/10.1103/PhysRevB.83.125201.
[22] Shin D, et al. (2016) $BaCu_2Sn(S,Se)_4$: Earth-abundant chalcogenides for thin-film photovoltaics. Chemistry of Materials 28:4771–4780. doi.org/10.1021/acs. chemmater. 6b01832.
[23] Blaha P, et al. (2020) WIEN2k: An APW+lo program for calculating the properties of solids. Journal of Chemical Physics 152:074101. doi.org/10.1063/1.5143061.
[24] Perdew JP, Burke K, Ernzerhof M (1996) Generalized gradient approximation made simple. Physical Review Letters 77:3865–3868. doi.org/10.1103/PhysRevLett.77.3865.
[25] Murnaghan FD (1944) The compressibility of media under extreme pressures. Proceedings of the National Academy of Sciences 30:244–247. doi.org/10.1 073/pnas.30.9.244.
[26] Marks LD (2013) Fixed-point optimization of atoms and density in DFT. Journal of Chemical Theory and Computation 9:2786–2800. doi.org/10.1021/ct4001685.
[27] Jaffe JE, Zunger A (1984) Theory of the band-gap anomaly in ABC2 chalcopyrite semiconductors. Physical Review B 29:1882–1906. doi.org/10.1103/PhysRevB.29.1882.
[28] Anisimov VI, et al. (1993) Density-functional theory and NiO photoemission spectra. Physical Review B 48:16929–16934. doi.org/10.1103/PhysRevB.48.16929.
[29] Liechtenstein AI, Anisimov VI, Zaanen J (1995) Density-functional theory and strong interactions: Orbital ordering in Mott–Hubbard insulators. Physical Review B 52:R5467–R5470. doi.org/10.1103/PhysRevB.52.R5467.
[30] Dudarev SL, et al. (1998) Electron-energy-loss spectra and the structural stability of nickel oxide: An LSDA+U study. Physical Review B 57:1505–1509. doi.org/10. 1103/PhysRevB.57.1505.
[31] Wyckoff RWG (1963) Crystal Structures, Vol. 1, 2nd ed. Interscience Publishers, New York.
[32] Rettig SJ, Trotter J (1987) Refinement of the structure of orthorhombic sulfur, α-S8. Acta Crystallographica Section C 43:2260–2262. doi.org/10.1107/S0108270187088152.
[33] Cherin P, Unger P (1967) The crystal structure of trigonal selenium. Inorganic Chemistry 6:1589–1591. doi.org/10.1021/ic50054a037.
[34] Gražulis S, et al. (2009) Crystallography Open Database – an open-access collection of crystal structures. Journal of Applied Crystallography 42:726–729. doi.org/10.1107/S0021 889809016690.
[35] Jain A, et al. (2011) Formation enthalpies by mixing GGA and GGA+U calculations. Physical Review B 84:045115. doi.org/10.1103/PhysRevB.84.045115.
[36] Ambrosch-Draxl C, Sofo JO (2006) Linear optical properties of solids within the full-potential linearized augmented planewave method. Computer Physics Communications 175:1–14. doi.org/10.1016/j.cpc.2006.03.005.
[37] ASTM International (2020) Standard Tables for Reference Solar Spectral Irradiances: Direct Normal and Hemispherical on 37° Tilted Surface. ASTM G173-03(2020), West Conshohocken, PA.
[38] Holmgren WF, et al. (2018) pvlib python: A Python package for modeling solar energy systems. Journal of Open Source Software 3:884. doi.org/10.21105/joss.00884.
[39] Shannon RD (1976) Revised effective ionic radii and systematic studies of interatomic distances in halides and chalcogenides. Acta Crystallographica Section A 32:751–767. doi.org/10.1107/S0567739476001551.
[40] Vegard L (1921) Die Konstitution der Mischkristalle und die Raumfüllung der Atome. Zeitschrift für Physik 5:17–26. doi.org/10.1007/BF01349680.

[41] Pearson RG (1963) Hard and soft acids and bases. Journal of the American Chemical Society 85:3533–3539. doi.org/10.1021/ja00905a001.
[42] Sun W, et al. (2016) The thermodynamic scale of inorganic crystalline metastability. Science Advances 2:e1600225. doi.org/10.1126/sciadv.1600225.
[43] Persson C (2010) Electronic and optical properties of Cu2ZnSnS4 and Cu2ZnSnSe4. Journal of Applied Physics 107:053710. doi.org/10.1063/1.3318468.
[44] Onida G, Reining L, Rubio A (2002) Electronic excitations: Density-functional versus many-body Green's-function approaches. Reviews of Modern Physics 74:601–659. doi.org/10.1103/RevModPhys.74.601.
[45] Rühle S (2016) Tabulated values of the Shockley–Queisser limit for single junction solar cells. Solar Energy 130:139–147. doi.org/10.1016/j.solener.2016.02.015.
[46] Yu L, Zunger A (2012) Identification of potential photovoltaic absorbers based on first-principles spectroscopic screening of materials. Physical Review Letters 108:068701. doi.org/10.1103/PhysRevLett.108.068701.